ADVANCED ENERGY MATERIALS
www.advenergymat.de

Low Onset-Potential Z-Scheme Ta_3N_5-based Photoanode with Enhanced Light Harvesting and Charge Transport

*Hee Ryeong Kwon, Jin Wook Yang, Sungkyun Choi, Woo Seok Cheon, In Hyuk Im, Younhwa Kim, Jungwon Park, Gwan-Hyoung Lee, and Ho Won Jang**

Simultaneous enhancement of light harvesting and charge transport in photoelectrochemical (PEC) systems is a major challenge to achieving high solar-to-hydrogen efficiency. Here, a Ta_3N_5-Si Z-scheme system is constructed to facilitate charge transport pathways from generation to catalysis, taking advantage of the exquisite bandgap and band position of Ta_3N_5. The tailored Ta_3N_5-Si junction with an NbN_x electron mediator effectively establishes a Z-scheme charge transport and enhances the driving force for water oxidation, reducing the onset potential by an increment in photovoltage. Moreover, the nitrogen-doped $CoFeO_x$ co-catalyst boosts hole dynamics and kinetics at the surface level, resulting in improved hole extraction for water oxidation catalysis. The synergy between the above strategies cooperatively expedites the charge separation and transport in a Ta_3N_5 photoanode, which decreases the photocurrent onset potential from 0.69 to 0.27 V versus the reversible hydrogen electrode, a reduction of 420 mV. This result represents one of the lowest onset potentials observed for Ta_3N_5-based photoanodes. A systematic approach to enhancing photovoltage and photocurrent expands the design concept of metal nitride-based PEC devices.

1. Introduction

Photoelectrochemical (PEC) water splitting, converting solar energy into hydrogen fuel, represents a sustainable way to diminish reliance on fossil fuels and switch toward low-carbon fuels.[1–3] The advancement of photoanode materials faces a pivotal challenge concerning the photogeneration of charge carriers and their acceleration within the kinetically slow multistep oxygen evolution reaction (OER).[4–6] Tackling this issue primarily revolves around semiconductor light absorbers with two key objectives: augmenting the quantum efficiency of photons to extend light harvesting and reducing recombination losses along the entire charge carrier pathway. There has been an effort to develop photoanode materials that extend light absorption into the visible spectrum.[7] Among photoanode candidates, Ta_3N_5 fulfills the criteria for a photoanode owing to its narrow bandgap of 2.1 eV and the appropriate band position that aligns with the water redox potentials. Various approaches, including doping,[8] nanostructuring,[9] and oxygen evolution co-catalysts (OECs),[10] have significantly enhanced the PEC activity of Ta_3N_5, especially in the photocurrent density (J_{ph}). Nevertheless, the onset potential (V_{on}) displays a substantial delay, typically reported in the range of 0.5–0.8 V versus the reversible hydrogen electrode (V_{RHE}).[11,12] Compared to the flat band potential of Ta_3N_5 (≈0 V_{RHE}), the actual V_{on} is considerably more positive than the ideal case.[7]

Essentially, the critical determinants of V_{on} are the energetics of semiconductors and the kinetics of surfaces.[13] However, Ta_3N_5 has been hampered by inherently short hole diffusion lengths, low OER activity, and susceptibility to photo-corrosion, leading to low photovoltage (V_{ph}), and significant overpotential. To achieve low V_{on}, Ta_3N_5 photoanodes have implemented various strategies to increase V_{ph} and decrease overpotential simultaneously. For instance, functional layers serving as charge transport (GaN,[14] NbN_x[15]), surface passivation (AlO_x,[16] TiO_x[17]), and hole storage (Fh[18]) can further increase V_{ph} by boosting charge separation efficiency. Furthermore, OEC modifications, such as $NiFeO_x$,[19] NiCoFe-B_i,[20] and $Co(OH)_2$,[21] effectively reduce the overpotential by providing abundant catalytic active sites and prolonging hole lifetimes. These findings highlight the importance of constructing an efficient charge transport path in photoanodes to advance V_{on} and J_{ph}.

Integrated tandem devices can drive water splitting by connecting light absorbers with different bandgaps to combine their respective photovoltages.[22] These offer the advantage of

H. R. Kwon, J. W. Yang, S. Choi, W. S. Cheon, I. H. Im, G.-H. Lee, H. W. Jang
Department of Materials Science and Engineering Research Institute of Advanced Materials
Seoul National University
Seoul 08826, Republic of Korea
E-mail: hwjang@snu.ac.kr
Y. Kim, J. Park
School of Chemical and Biological Engineering and Institute of Chemical Processes
Seoul National University
Seoul 08826, Republic of Korea
H. W. Jang
Advanced Institute of Convergence Technology
Seoul National University
Suwon 16229, Republic of Korea

The ORCID identification number(s) for the author(s) of this article can be found under https://doi.org/10.1002/aenm.202303342

DOI: 10.1002/aenm.202303342

utilizing separate absorption regions to harness the entire solar spectrum, placing the top, and bottom light absorbers in a single path. Hence, the photon flux needs to be distributed adequately to each light absorber to maximize the PEC efficiencies. Theoretically, the optimal bandgaps for the top and bottom absorbers have been calculated to be 1.8 and 1.1 eV, respectively.[23,24] From this perspective, silicon (Si) with a bandgap of 1.12 eV is considered an excellent material for the bottom absorber. At that point, extensive research has been conducted on Si heterojunctions, including TiO_2/Si,[25,26] Fe_2O_3/Si,[27–29] WO_3/Si,[30,31] and Ta_3N_5/Si.[32] This structure can complement the delayed onset of a Si photoanode and the limited absorption region of metal oxide and nitride photoanodes cooperatively.

Distinctively, a dual absorber photoanode operates using a Z-scheme mechanism, analogous to the electron flow from photosystem II to photosystem I in natural photosynthesis.[33,34] In this system, the photogenerated holes from the top absorber are utilized in the OER, while the photogenerated electrons from the bottom absorber are directed to the counter electrode for the hydrogen evolution reaction. This operation isolates active carriers for specific redox reactions and achieves charge balance by vectorial transfer of electrons generated in the top absorber and holes generated in the bottom absorber.[29] It should be noted that these charge transport pathways can also promote charge separation through electron-hole recombination at the interface between each light absorber.[25,35] Moreover, the all-solid-state Z-scheme, which inserts a metallic electron mediator at the interface of two light absorbers, has further enhanced charge separation and transport.[36,37] Using this approach, the WO_3-Si heterojunction exhibited increased V_{ph} and a cathodic shift in V_{on} via an electron mediator with a controlled work function.[30] The reported WO_3/Pt/Si photoanode suggests the importance of increasing Si band bending to utilize the V_{ph} of Si effectively.

Here, we design a novel strategy to enhance the PEC performance of a Ta_3N_5 photoanode by introducing the Ta_3N_5-Si heterojunction and OEC design. Specifically, we aim to address the high onset potential of Ta_3N_5, with an emphasis on two aspects: heterojunction structure at the bulk level and the hole dynamics and kinetics at the surface level. We successfully fabricate the Ta_3N_5/NbN_x/Si photoanode by integrating a Ta_3N_5 top light absorber, a Si bottom light absorber, and an NbN_x electron mediator. This configuration enables us to establish a Z-scheme charge transport channel and achieve the ideal bandgap alignment in our two-photon devices. Subsequently, the photovoltage contributions from each light absorber, which lead to the advancement of the onset potential, are untangled. The resulting Ta_3N_5/NbN_x/Si, modified with a thin and uniform N-doped $CoFeO_x$ (denoted as N:$CoFeO_x$) co-catalyst, enhances the J_{ph} and V_{on} additionally. The modulation of electron configuration due to N species played a crucial role in the lifetime of holes and catalytic activity. By combining the integrated light absorber and OEC design, the N:$CoFeO_x$/Ta_3N_5/NbN_x/Si photoanode yields a remarkable water oxidation onset potential of 0.27 V_{RHE} and a photocurrent density of 9.28 mA cm^{-2} at 1.23 V_{RHE}. These results demonstrate that efficient light absorber design and maximization of energetics and kinetics are competitive strategies for enhancing PEC activity. This may also provide insights into the systematic development of metal nitride-based tandem systems for high-performance solar water splitting.

2. Results and Discussion

2.1. Ta_3N_5-Si Heterojunction with an NbN_x Interlayer

To investigate the heterojunction structure of Ta_3N_5 and Si with and without an NbN_x interlayer, two different structures were fabricated: Ta_3N_5/NbN_x/n-Si and Ta_3N_5/n-Si. First, Nb_2O_5 and Ta_2O_5 films were deposited as oxide precursors on the etched n-Si substrate by electron-beam evaporation (Figure S1, Supporting Information). Subsequently, a one-step nitridation process was carried out in an ammonia atmosphere at 950 °C, during which oxygen was substituted with nitrogen, forming highly crystalline nitride phases. The scanning electron microscope (SEM) image of the surface morphologies of Ta_3N_5 shows grains distributed several hundred nanometers and tiny pores formed on the surface after thermal nitridation (**Figure 1a**). According to the cross-sectional SEM image in Figure 1b, the NbN_x and Ta_3N_5 films formed a well-integrated heterojunction structure on the n-Si substrate. The thickness of the Ta_3N_5 layer was controlled to 620 nm to ensure sufficient absorption efficiency as a light absorber. As an electron mediator in the heterostructures, the NbN_x layer inserted between Ta_3N_5 and n-Si was optimized to a thickness of ≈20 nm. The thickness of the mediator determines the optical transmittance and electrical resistance in heterostructures that integrate two semiconductors. Transmission electron microscopy (TEM) images of the Ta_3N_5/NbN_x/n-Si and Ta_3N_5/n-Si (Figure S2a,b, Supporting Information) indicate that the Ta_3N_5 layer also formed a well-adhered film on the n-Si substrate in the Ta_3N_5/n-Si without the NbN_x interlayer.

An X-ray diffraction (XRD) analysis was conducted to explore the crystal structure of the Ta_3N_5 and NbN_x films. The diffraction peaks of the Ta_3N_5/NbN_x/n-Si and Ta_3N_5/n-Si are consistent with the orthorhombic Ta_3N_5, as shown in Figure 1c. Under the nitridation condition, the single-phase Ta_3N_5 crystal structure was obtained without oxynitride phases and impurity phases. The crystallinity of Ta_3N_5 was well maintained, independent of the existence of the NbN_x interlayer. The crystalline phase of the NbN_x layer was interpreted using XRD patterns from the NbN_x film obtained by nitridating Nb_2O_5/n-Si (Figure 1d), as the diffraction peaks overlapped with those of Ta_3N_5. The diffraction peaks of NbN_x are in good agreement with the tetragonal Nb_4N_5. The coexistence of the NbN_x (x<1) phase is also apparent, as evidenced by a peak at 32.5°. This is attributed to the tendency of Nb^{5+} to be reduced to a lower valence state, which determines the crystalline phase of NbN_x formed during the nitridation process.[38] As corroborated by XRD analysis, high-resolution TEM (HR-TEM) images in Figure 1e–g clearly demonstrate the crystallinity of Ta_3N_5 and NbN_x phases in their respective regions. The notable observation is that, as evident from Figure 1e, at the interface between Ta_3N_5 and NbN_x, the two nitrides maintain high crystallinity and establish intimate contact. In contrast, at the interface of Ta_3N_5/n-Si, an amorphous layer with a few nanometers of thickness was observed (Figure S3, Supporting Information). In Figure 1f,g, the HR-TEM images from each specific region show explicit lattice spacings, which are indexed to the crystal planes of Ta_3N_5 and Nb_4N_5. The corresponding selected area electron diffraction (SAED) patterns from each region are displayed on the right side of Figure 1f,g, wherein the measured interplanar

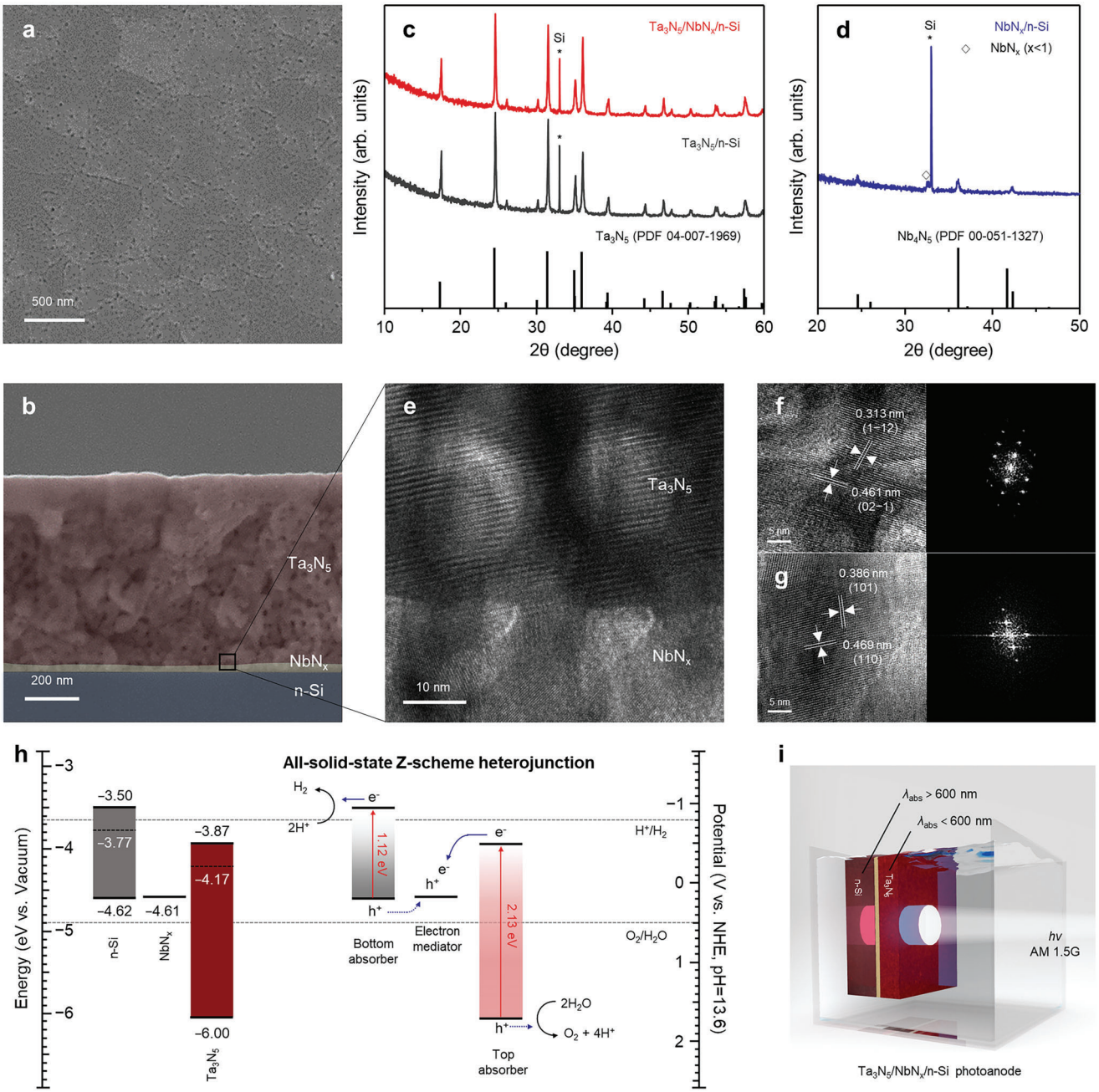

Figure 1. a, b) Top and cross-sectional SEM images of the $Ta_3N_5/NbN_x/n$-Si. XRD patterns for c) Ta_3N_5/NbN_x and Ta_3N_5 films, and d) NbN_x film on n-Si substrates synthesized by e-beam evaporation and one-step nitridation. e) HR-TEM image of the Ta_3N_5/NbN_x interface. HR-TEM images and SAED patterns of f) the Ta_3N_5, and g) the NbN_x regions. h) Experimentally determined energy band diagrams of n-Si, NbN_x, , and Ta_3N_5. i) Illustration of the Z-scheme $Ta_3N_5/NbN_x/n$-Si photoanode.

distances of 0.313 and 0.461 nm are ascribed to the (1–12) and (02-1) planes of Ta_3N_5, respectively (Figure 1f). In Nb_4N_5, the interplanar distances of 0.469 and 0.386 nm are ascribed to the (110) and (101) planes, respectively (Figure 1g).

To elucidate the energy band energetics of the heterojunction, we analyzed the band structure of the two n-type semiconductors, Ta_3N_5 and n-Si, along with the metallic NbN_x layer that acts as an electron mediator. The surface electronic structures of Ta_3N_5, NbN_x, and n-Si were obtained through ultraviolet photoelectron spectroscopy (UPS) (Figure S4a,b, Supporting Information). From the UPS results, the Fermi level (E_f) of Ta_3N_5 and n-Si was calculated to be 4.17 and 3.77 eV. The work function of NbN_x was determined to be 4.61 eV, exhibiting a notable difference from the E_f of both n-type semiconductors, particularly a significant difference from the E_f of n-Si. The derived valence band maximum (E_{VBM}) of Ta_3N_5 and n-Si was positioned at 4.62 and 6.00 eV, respectively. Furthermore, the bandgap of Ta_3N_5 was determined using the Tauc plot and found to be 2.13 eV,

which was similar to the reported value (Figure S5, Supporting Information).[39] The detailed energy band diagrams of Ta_3N_5, NbN_x, and n-Si and all-solid-state Z-scheme charge flow are illustrated in Figure 1h. In Ta_3N_5/NbN_x/n-Si with a tailored NbN_x electron mediator, two light absorbers can absorb the split wavelengths to maximize the light-harvesting efficiency (Figure 1i).

2.2. Light Harvesting and Charge Transport in Ta_3N_5/NbN_x/n-Si

Based on the band structure analysis, the behavior of the dual absorber system in the Ta_3N_5-Si heterojunction was investigated. Without an NbN_x interlayer, Ta_3N_5/n-Si has a band structure capable of the Z-scheme charge transport concept described above (Figure S6a, Supporting Information). The PEC water oxidation activity of the Ta_3N_5/n-Si was evaluated in 1 M KOH using a conventional three-electrode system with CoO_x co-catalyst modification (Figure S6b, Supporting Information). The Ta_3N_5/n-Si exhibited optimized photocurrent density at a thickness of 80 nm for Ta_3N_5. The assessment was conducted in the same manner for the Ta_3N_5/n^+-Si, where the doping level of Si was increased to eliminate the light absorption effect of n-Si. The onset potential of Ta_3N_5/n-Si exhibited a cathodic shift of ≈200 mV compared to Ta_3N_5/n^+-Si, confirming the effectiveness of the dual absorber system (Figure S6c, Supporting Information). However, the overall low photocurrent density of Ta_3N_5/n-Si suggests that introducing an electron mediator layer is necessary to exploit the Z-scheme charge flow extensively. In the Ta_3N_5-Si heterojunction, there is a clear need for a contact layer that can maximize the band bending of n-Si to utilize the V_{ph} of n-Si and facilitate efficient back electron transport in Ta_3N_5.[40]

Subsequently, Ta_3N_5/NbN_x/n-Si, introducing a 20 nm NbN_x interlayer, demonstrated a noticeable improvement in photocurrent density and lower charge transport resistance (Figure S7a,b, Supporting Information). As shown in Figure S3 (Supporting Information), the relatively thick amorphous layer formed between Ta_3N_5 and n-Si during the nitridation process can hinder charge transport and serve as the primary recombination path, thus impeding the efficient movement of charge carriers in the Ta_3N_5/n-Si. Furthermore, the exceptional charge transport properties of NbN_x also support the reduced resistance (Figure S7c, Supporting Information). In the electrolyte containing the electron scavenger, NbN_x exhibited a faster onset potential and higher current compared to Si with a native oxide surface. Above all, the most significant difference is attributed to the band-bending effect induced by NbN_x. In the Ta_3N_5/NbN_x/n-Si structure, the NbN_x interlayer served as a charge carrier mediator and, with its high work function of 4.61 eV, increased the Schottky barrier at the n-Si. The proposed band bending of n-Si by NbN_x is evidenced by the difference in the flat band potential observed in the Mott-Schottky analysis (Figure S7d, Supporting Information). The flat band potential of Ta_3N_5/NbN_x/n-Si was −0.18 V_{RHE}, which is 0.16 V_{RHE} lower than Ta_3N_5/n-Si. In other words, compared to the direct Z-scheme of Ta_3N_5/n-Si, the NbN_x-mediated Z-scheme heterojunction in Ta_3N_5/NbN_x/n-Si indicates an enhanced charge transport via charge matching interlayer. This Z-scheme with electron mediator facilitates the individual separation and utilization of photogenerated charges in both light absorbers.

To increase the absorption of Ta_3N_5, the thickness of Ta_3N_5 was increased to 620 nm to form a Ta_3N_5/NbN_x/n-Si structure. As shown in **Figure 2a**, the photocurrent density of the Ta_3N_5/NbN_x/n-Si with the NbN_x thickness optimized to 20 nm was 6.64 mA cm^{-2} at 1.23 V_{RHE} under AM 1.5G simulated full spectrum. On the one hand, to ensure sufficient light absorption in the bottom absorber, the thickness of the NbN_x needs to be kept thin. On the other hand, to serve as an electron mediator, a certain level of thickness is required to achieve the appropriate conductivity. Therefore, the optimal point where these two characteristics are balanced was determined by adjusting the thickness of the NbN_x film (Figure S8, Supporting Information). Subsequently, PEC measurements were performed using an optical filter that allowed the short-wavelength region below 600 nm and the long-wavelength region above 600 nm to pass under AM 1.5G illumination. When light with wavelengths below 600 nm was irradiated, photoexcitation occurred only in Ta_3N_5. The generated electrons required a higher anodic bias to traverse the conduction band of n-Si, leading to a anodic shift in the onset potential than full spectrum illumination (Figure 2a). Conversely, when light with wavelengths above 600 nm was irradiated, sufficient driving force was not provided for the photogenerated holes from n-Si to pass through the upper Ta_3N_5 and participate in OER (Figure 2a). While the photocurrent due to the absorption of n-Si was minuscule, the photocurrent was enhanced under the absorption of both light absorbers. This clearly demonstrates that the behavior of the two light absorbers exhibits a Z-scheme heterojunction rather than a Type II heterojunction. The photogenerated charges in n-Si indirectly contribute to the fast photocurrent response by harnessing the residual light that penetrates through Ta_3N_5. Despite the charge transport delays caused by the Schottky barrier between Ta_3N_5 and NbN_x, the dominant effect remains the enhancement of photogenerated charge separation and V_{ph} in n-Si.[30] To assess the photon flux in the dual absorber photoanode, the optical properties were examined at the optimized thickness on the quartz substrate. Figure 2b illustrates that the absorption of Ta_3N_5 exhibits ≈75% up to 580 nm, and the transmitted light through Ta_3N_5/NbN_x reaches ≈35% in the wavelength range from 600 to 1200 nm. In the absorbance spectrum for Ta_3N_5/NbN_x/n-Si, it was confirmed that absorbance for both Ta_3N_5 and n-Si occurred. Significant fluctuation appeared at wavelengths above 600 nm due to the interference effect of Ta_3N_5/NbN_x (Figure S9a, Supporting Information). Optically translucent NbN_x ensured the light absorption of the bottom absorber and allowed the construction of the light pathway (Figure S9b, Supporting Information).

An identical configuration was established using n^+-Si, investigating both the rearward movement of electrons from Ta_3N_5 through NbN_x to n^+-Si and the light absorption of n-Si in the presence of NbN_x (Figure 2c). The photocurrent density at 1.23 V_{RHE} of the $Ta_3N_5/NbN_x/n^+$-Si was 4.26 mA cm^{-2}, supporting the formation of an efficient electron pathway through the NbN_x interlayer compared to the structure without interlayer. The current density-applied potential (J–V) characteristics of $Ta_3N_5/NbN_x/n^+$-Si are comparable to those of the light illumination below 600 nm in Figure 2a. A more detailed comparison between n-Si and n^+-Si reveals that the intensified band bending of n-Si due to the Schottky contact with NbN_x led to a cathodic shift of the onset potential. According to the first order derivative method,[41,42]

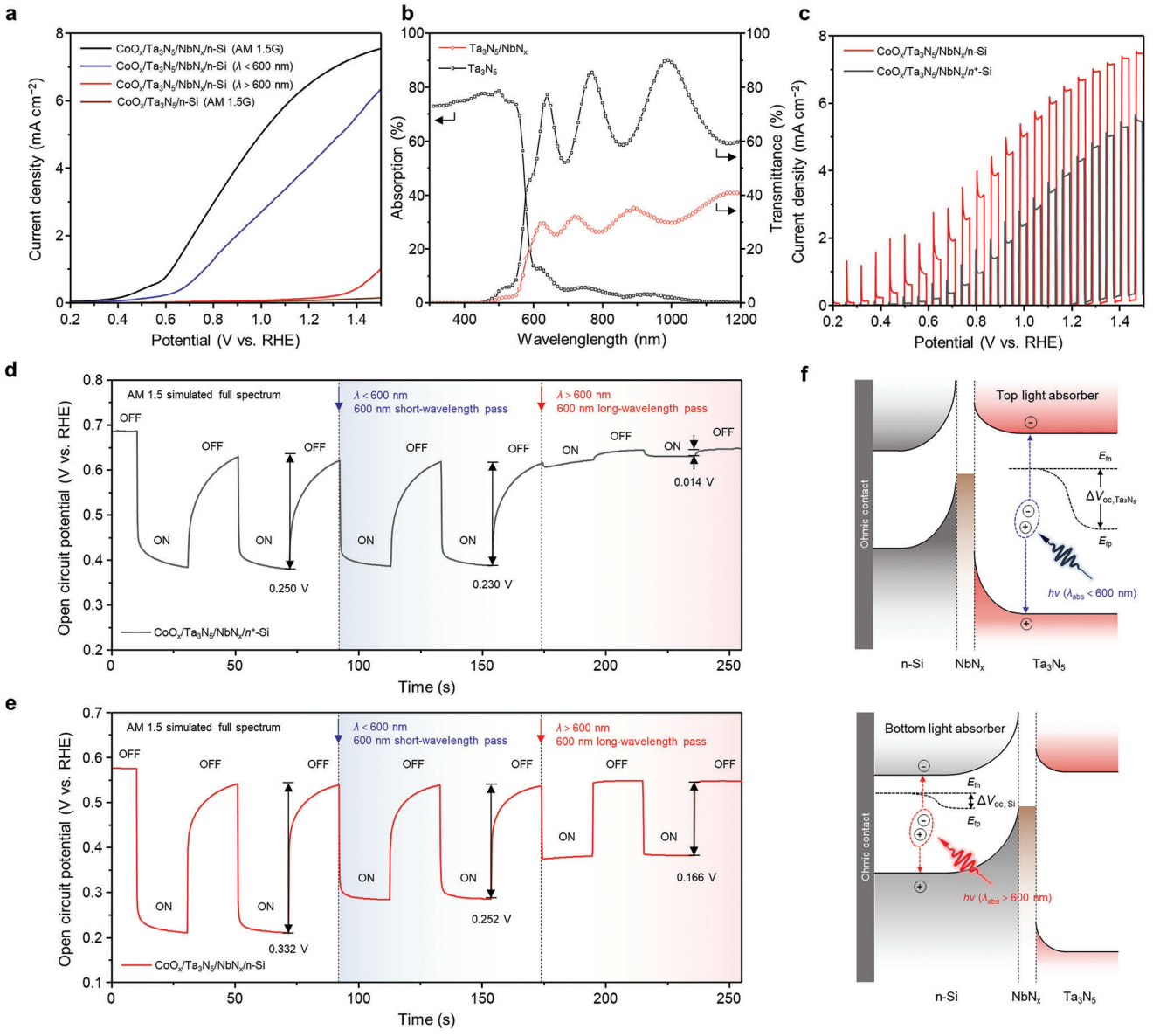

Figure 2. a) *J–V* curves of $Ta_3N_5/NbN_x/n$-Si with CoO_x co-catalyst in 1 M KOH under AM 1.5G illumination, with a 600 nm short-wavelength pass filter and a 600 nm long-wavelength pass filter. b) UV–vis absorption and transmittance spectra of Ta_3N_5/NbN_x and Ta_3N_5 films on quartz substrates. c) *J–V* curves of $CoO_x/Ta_3N_5/NbN_x$/n-Si and $CoO_x/Ta_3N_5/NbN_x/n^+$-Si under chopped AM 1.5G illumination. Open circuit potential (V_{oc}) versus elapsed time under chopped AM 1.5G illumination with a 600 nm short-wavelength pass filter and a 600 nm long-wavelength pass filter for d) $CoO_x/Ta_3N_5/NbN_x/n^+$-Si, and e) $CoO_x/Ta_3N_5/NbN_x$/n-Si. f) Energy band diagrams of the Ta_3N_5/NbN_x/n-Si photoanode under different wavelength illuminations.

the Ta_3N_5/NbN_x/n-Si improved the onset potential to 0.41 V_{RHE}, which was reduced by 280 mV compared to the $Ta_3N_5/NbN_x/n^+$-Si (Figure S10, Supporting Information). In the chopped *J–V* curves, a transient photocurrent decay at 0.2–0.4 V_{RHE} was also observed only in Ta_3N_5/NbN_x/n-Si, suggesting the capability to extract photogenerated holes.

To scrutinize the V_{ph} distribution between Ta_3N_5 and n-Si, the open circuit potential (V_{oc}) measurements were conducted under filtered light illumination. In Figure 2d, when AM 1.5G full spectrum illumination was applied, the ΔV_{oc} of $Ta_3N_5/NbN_x/n^+$-Si between the light on and off states was 0.250 V, and comparable ΔV_{oc} of 0.230 V was observed under chopped illumination with a 600 nm short wavelength pass filter. The ΔV_{oc} was only 0.014 V under chopped illumination with a 600 nm long wavelength pass filter, which was explained by the absorption by defect states in Ta_3N_5.[43] As displayed in Figure 2e, the ΔV_{oc} of Ta_3N_5/NbN_x/n-Si was 0.332 V, indicating an increased V_{ph}. When decoupling the individual contributions of each light absorber, the ΔV_{oc} of Ta_3N_5 was 0.252 V, and ΔV_{oc} of n-Si was 0.166 V. Meanwhile, the ΔV_{oc} under full spectrum was smaller than the sum of ΔV_{oc} of Ta_3N_5 and n-Si, which is attributed to the simultaneous upward shift of the E_f in the photoexcited states of both light absorbers. Additionally, this contrasts starkly with the ΔV_{oc} observed under the 600 nm long wavelength illumination for Ta_3N_5/n-Si in

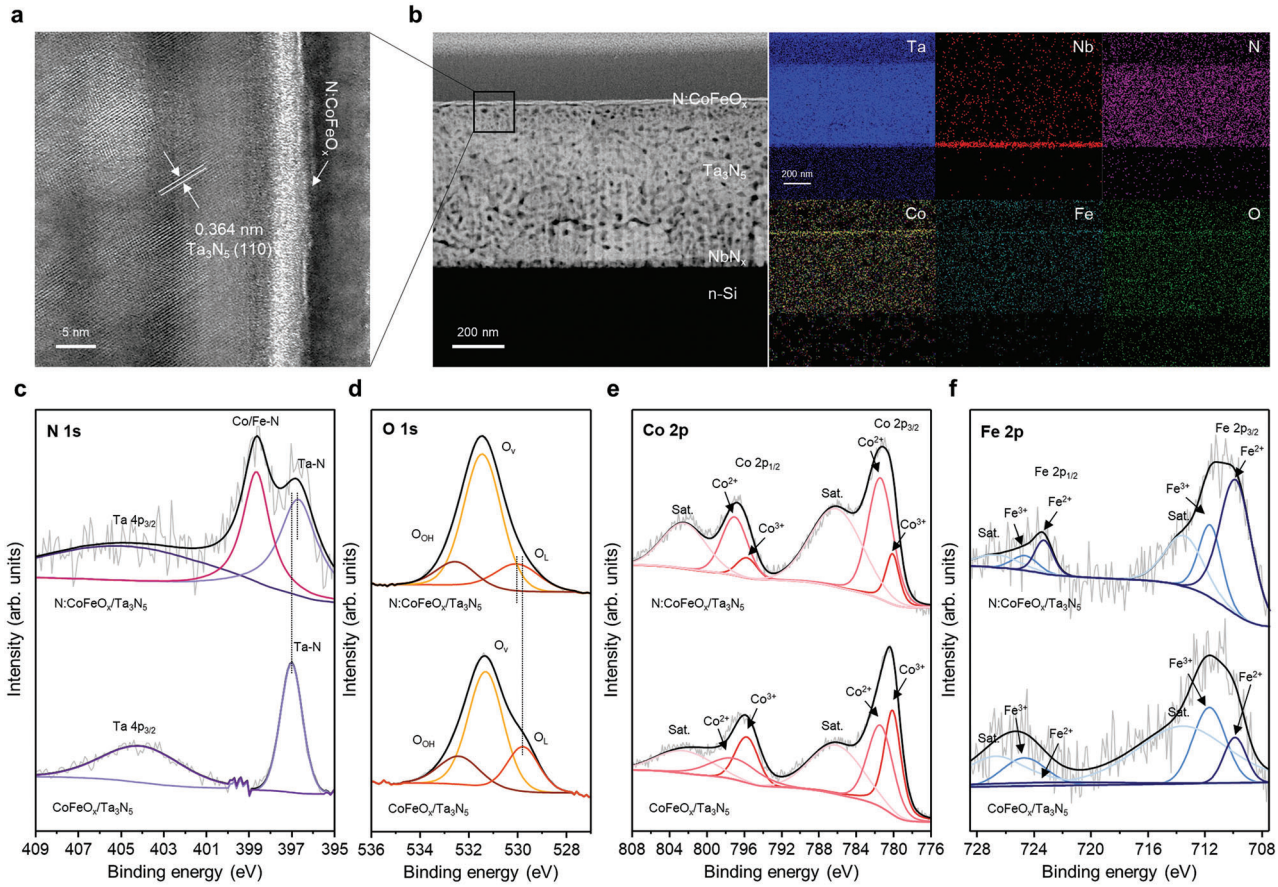

Figure 3. a) Cross-sectional HR-TEM image of N:CoFeO$_x$/Ta$_3$N$_5$/NbN$_x$/n-Si. B) Cross-sectional STEM image and corresponding EDX elemental mappings of N:CoFeO$_x$/Ta$_3$N$_5$/NbN$_x$/n-Si. XPS spectra: c) N 1s, d) O 1s, e) Co 2p, and f) Fe 2p of N:CoFeO$_x$/Ta$_3$N$_5$/NbN$_x$/n-Si and CoFeO$_x$/Ta$_3$N$_5$/NbN$_x$/n-Si.

Figure S11 (Supporting Information). A spike-shaped curve appeared in the absence of NbN$_x$, confirming the inability to form effective photovoltage by n-Si. Figure 2f shows the energy band diagrams illustrating the process of V_{ph} formation from each light absorber. When irradiated with wavelengths below 600 nm, the electron and hole pairs generated in Ta$_3$N$_5$ are separated to form the electron quasi-Fermi level (E_{fn}) and the hole quasi-Fermi level (E_{fp}), respectively, and the difference contributes to the ΔV_{oc} of Ta$_3$N$_5$. On the other hand, light with wavelengths above 600 nm transmitted through Ta$_3$N$_5$/NbN$_x$ induces photoexcited electron and hole pairs to develop in n-Si, adding to a ΔV_{oc} of n-Si equal to the disparity between E_{fn} and E_{fp}. In this manner, splitting the photon flux utilizes the two distinct light absorbers efficiently. Furthermore, the electrons and holes individually generated by these absorbers follow a charge flux based on the Z-scheme, thereby substantially elevating the voltage throughout the entire circuit and yielding increased photocurrent.

2.3. Structure Analysis of N:CoFeO$_x$/Ta$_3$N$_5$/NbN$_x$/n-Si

To further enhance the water oxidation kinetics on the surface of the Ta$_3$N$_5$ absorber, a strategy involving chemical composition adjustment and anion defect engineering was employed. Derived from the CoO$_x$-modified Ta$_3$N$_5$/NbN$_x$/n-Si (denoted as CoO$_x$/Ta$_3$N$_5$), the CoFeO$_x$-modified Ta$_3$N$_5$/NbN$_x$/n-Si (denoted as CoFeO$_x$/Ta$_3$N$_5$) was optimized with a chemical composition including 25% Fe to maximize photocurrent generation (Figure S12, Supporting Information). The N:CoFeO$_x$-modified Ta$_3$N$_5$/NbN$_x$/n-Si photoanode (denoted as N:CoFeO$_x$/Ta$_3$N$_5$) was obtained through the introduction of nitrogen species into the CoFeO$_x$/Ta$_3$N$_5$ via moderate N$_2$ plasma doping. As shown in **Figure 3a**, the N:CoFeO$_x$ OEC layer with a thickness of 5 nm was uniformly and conformally coated on the Ta$_3$N$_5$ surface. The HR-TEM image indicates an amorphous N:CoFeO$_x$ layer and a crystallized Ta$_3$N$_5$ with a lattice parameter of 0.364 nm corresponding to the (110) planes, which was in accordance with the XRD analysis. Figure 3b displays the scanning transmission electron microscopy (STEM) image of the final N:CoFeO$_x$/Ta$_3$N$_5$ photoanode structure and the corresponding energy-dispersive X-ray spectroscopy (EDX) mapping. The EDX mapping demonstrates the homogeneous distribution of Ta, Nb, and N elements within their respective Ta$_3$N$_5$ and NbN$_x$ films. In addition, the major elements of the OEC layer, Co, Fe, O, and N, exhibit predominant signals on the surface of Ta$_3$N$_5$.

X-ray photoelectron spectroscopy (XPS) was conducted to analyze the surface chemical states of the N:$CoFeO_x$/Ta_3N_5 photoanode. In the survey spectra, signals corresponding to Ta, N, Co, Fe, and O were all detected (Figure S13, Supporting Information). In Figure 3c, the high-resolution XPS spectrum of N 1s confirms the formation of Co/Fe-N bonding with a peak at 398.8 eV in N:$CoFeO_x$/Ta_3N_5, consistent with previously reported results.[44] Additionally, the binding energy of both N 1s and Ta 4f in Ta_3N_5 shifted to a low binding energy region compared with $CoFeO_x$/Ta_3N_5 in Figure 3c and Figure S14 (Supporting Information), indicating effective electron transfer from N:$CoFeO_x$ to Ta_3N_5.[45] In conjunction with the HR-TEM image (Figure 3a), this observation provides strong evidence of the successful formation of N:$CoFeO_x$/Ta_3N_5 photoanode. In Figure 3d, the O 1s spectrum exhibited three well-fitted peaks located at 529.8, 531.3, and 532.5 eV that were assigned to the lattice oxygen (O_L), oxygen vacancy (O_v), and hydroxyl oxygen (O_{OH}), respectively. The N incorporation in $CoFeO_x$ leads to the positive direction shift in the binding energy of O 1s. Simultaneously, the decrease in O_L peak intensity in N:$CoFeO_x$/Ta_3N_5 demonstrates the conversion of O bonding to N bonding. Moreover, the XPS spectra of Co 2p and Fe 2p were deconvoluted into spin-orbit doublets and shakeup satellites of $2p_{3/2}$ and $2p_{1/2}$ (Figure 3e,f). The Co $2p_{3/2}$ spectra were fitted with two peaks at 780.1 and 781.5 eV, and the Co $2p_{1/2}$ spectra were fitted with two peaks at 795.7 and 797.1 eV, corresponding to Co^{3+} and Co^{2+}, respectively (Figure 3e).[46] Similarly, the Fe $2p_{3/2}$ spectra were fitted with two peaks at 709.9 and 711.7 eV, and the Fe $2p_{1/2}$ spectra were fitted with two peaks at 723.3 and 724.8 eV, corresponding to Fe^{2+} and Fe^{3+}, respectively (Figure 3f).[47] Notably, the relative ratio of Co^{2+}/Co^{3+} and Fe^{2+}/Fe^{3+} increased in N:$CoFeO_x$/Ta_3N_5 with the coexistence of divalent and trivalent states. Due to substitution defects of nitrogen, which has a lower electronegativity than oxygen, the N:$CoFeO_x$ layer incorporates Co and Fe sites with higher electron densities. On the basis of electron enrichment features, transition metal sites with low-valence states are well-known for their exceptional electron transport performance, boosting water oxidation electrocatalytic activity.[48–50] Hence, the N:$CoFeO_x$ with increased concentrations of Co^{2+} and Fe^{2+} can offer abundant active sites and effectively lower the catalytic overpotential. Furthermore, the charge storage ability in the low-valence state of Co can extend the hole lifetime, reducing recombination, and increasing the probability of the photogenerated holes participating in the OER.[51] Overall, the electron configuration tuned by N-element substitution provides the advantages of excellent OER kinetics and superior hole dynamics, which can enhance PEC activity in water oxidation.

2.4. PEC Performance with N:$CoFeO_x$ Co-Catalyst

The PEC water oxidation performance of the OEC/Ta_3N_5 junction was measured in 1 M KOH under AM 1.5G illumination. As shown in **Figure 4a**, the $CoFeO_x$/Ta_3N_5 photoanode exhibits an increased photocurrent density of 7.48 mA cm^{-2} at 1.23 V_{RHE}, which is a 13% improvement compared to the CoO_x/Ta_3N_5 photoanode (6.64 mA cm^{-2} at 1.23 V_{RHE}). Demonstrating the additional effect of N-atom incorporation, the N:$CoFeO_x$/Ta_3N_5 photoanode shows an impressive photocurrent density of 9.27 mA cm^{-2} at 1.23 V_{RHE}, a notable 40% enhancement over the CoO_x/Ta_3N_5 photoanode. Another noteworthy feature is that the N:$CoFeO_x$/Ta_3N_5 photoanode shows a markedly low onset potential of 0.27 V_{RHE} when evaluating the onset potential at a photocurrent density of 0.2 mA cm^{-2} (Figure 4b).[52] The composition tuning with Fe expedited the onset potential, leading to a 60 mV shift. Consecutively, incorporating nitrogen elements made this rapid onset potential possible, leading to a further 70 mV shift. A similar tendency is confirmed in the onset potential obtained through the first-order derivatives of the *J–V* curves (Figure S15, Supporting Information). In addition, to better comprehend the effect of N_2 plasma treatment, we examined its impact on the PEC properties of Ta_3N_5 and CoO_x/Ta_3N_5 (Figure S16a,b, Supporting Information). The controlled plasma conditions had little impact on the *J–V* characteristics of Ta_3N_5 photoanode. At the same time, N:CoO_x/Ta_3N_5 exhibited an improved photocurrent density of 6.68 mA cm^{-2} at 1.23 V_{RHE} compared to before plasma treatment. Nevertheless, the functionality of N species was found to be superior when applied to dual metal oxide compared to single metal oxide.

The stability evaluation of the OEC/Ta_3N_5 photoanodes for water oxidation was conducted by examining the *J–t* curves at constant 1.23 V_{RHE} (Figure S17, Supporting Information). The photocurrent of Ta_3N_5 decreased rapidly at first due to severe photo-corrosion, as reported previously.[53] However, the N:$CoFeO_x$/Ta_3N_5 photoanode was more resistant to photocorrosion than other OEC layers, with a delay in the decrease of photocurrent. Moreover, oxygen and hydrogen evolution by the N:$CoFeO_x$/Ta_3N_5 photoanode and Pt cathode were detected using gas chromatography (Figure S18, Supporting Information). Faradaic efficiencies (FE) were evaluated, representing the efficiency of charge participation in the target electrochemical reactions. The calculated FE of N:$CoFeO_x$/Ta_3N_5 photoanode reached ≈ 97%, proving that photogenerated holes are used for water oxidation. Based on this reliable FE value, the half-cell solar-to-hydrogen energy conversion efficiency (HC-STH) values were calculated (Figure 4c). The HC-STH of N:$CoFeO_x$/Ta_3N_5 reached a peak value of 1.82% at 0.87 V_{RHE}, a higher value at low applied potential than CoO_x/Ta_3N_5 (1.34% at 0.87 V_{RHE}).

Bulk separation and surface injection were determined in the same electrolyte with a hole scavenger, as described in the experimental section. Surface charge injection efficiency (η_{inj}), representing the capacity of hole transfer into the OER at the OEC/electrolyte interface, was calculated using *J–V* curves with a hole scavenger (Figure S19a, Supporting Information). As displayed in Figure 4d, the η_{inj} values were higher in the order of N:$CoFeO_x$/Ta_3N_5, $CoFeO_x$/Ta_3N_5, and CoO_x/Ta_3N_5 in the entire potential range. Specifically, N:$CoFeO_x$/Ta_3N_5 exhibited an η_{inj} of 50% from a low potential of 0.4 V_{RHE}, gradually increasing to over 80% at 1.4 V_{RHE}. This substantiates exceptional hole injection capability from low applied potentials, validating the rapid onset potential observed in previous *J–V* curves (Figure 4b). The derived bulk separation efficiency (η_{sep}) also showed that the N:$CoFeO_x$ co-catalyst recorded high values within the potential range (Figure S19b,c, Supporting Information). The η_{sep} value does not exhibit a significant difference between co-catalysts compared to η_{inj}. However, the difference in separation efficiency at 0.8 V_{RHE} clearly illustrates that N:$CoFeO_x$ can prevent recombination and enhance the reaction kinetics. To get more

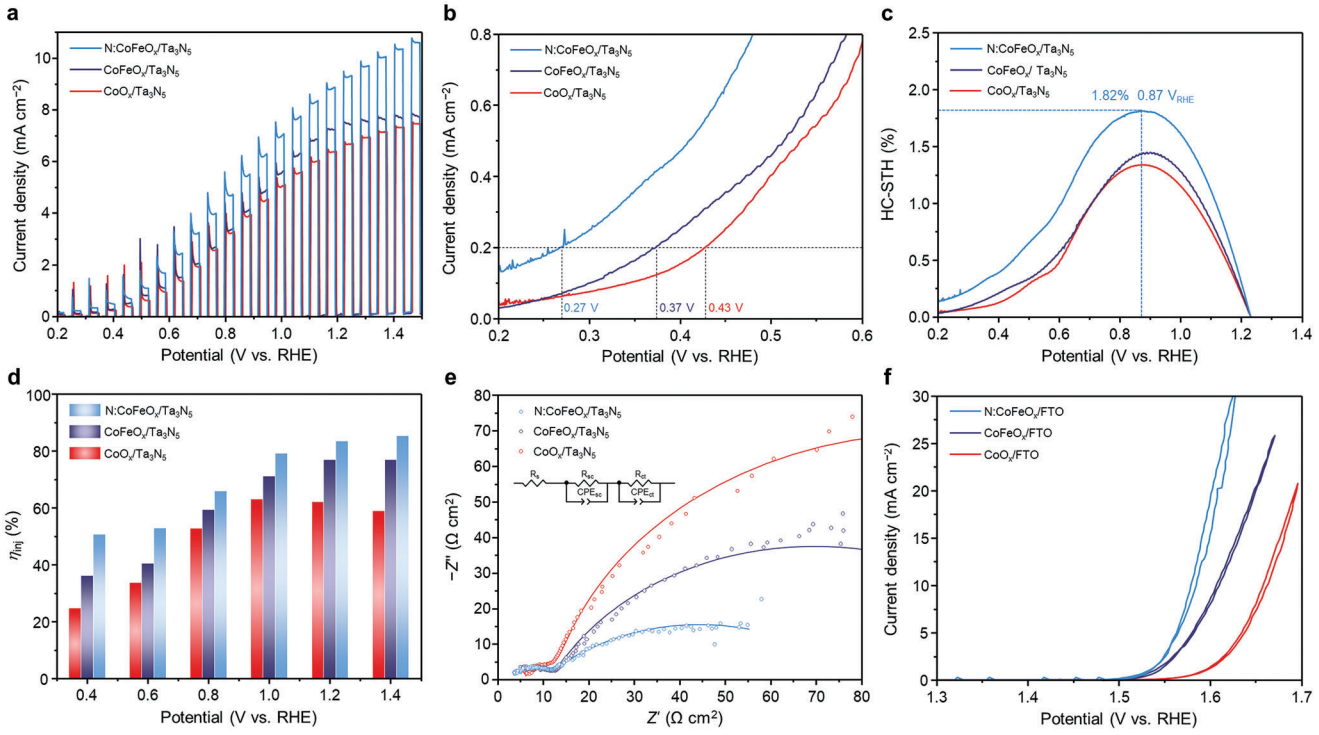

Figure 4. a) *J–V* curves of N:CoFeO$_x$/Ta$_3$N$_5$/NbN$_x$/n-Si, CoFeO$_x$/Ta$_3$N$_5$/NbN$_x$/n-Si, and CoO$_x$/Ta$_3$N$_5$/NbN$_x$/n-Si in 1 M KOH under chopped AM 1.5G illumination, b) Extracted onset potential of N:CoFeO$_x$/Ta$_3$N$_5$/NbN$_x$/n-Si, CoFeO$_x$/Ta$_3$N$_5$/NbN$_x$/n-Si, and CoO$_x$/Ta$_3$N$_5$/NbN$_x$/n-Si in *J–V* curves, c) HC-STH curves, d) Surface charge injection efficiencies (η_{inj}) of N:CoFeO$_x$/Ta$_3$N$_5$/NbN$_x$/n-Si, CoFeO$_x$/Ta$_3$N$_5$/NbN$_x$/n-Si, and CoO$_x$/Ta$_3$N$_5$/NbN$_x$/n-Si. e) Nyquist plots of EIS spectra at 1.23 V_{RHE} for N:CoFeO$_x$/Ta$_3$N$_5$/NbN$_x$/n-Si, CoFeO$_x$/Ta$_3$N$_5$/NbN$_x$/n-Si, and CoO$_x$/Ta$_3$N$_5$/NbN$_x$/n-Si. f) Cyclic voltammetry curves of N:CoFeO$_x$, CoFeO$_x$, and CoO$_x$ catalysts on FTO with *iR*-compensation under dark condition.

insights into the charge transfer kinetics of the photoanodes in the PEC water oxidation process, the electrochemical impedance spectroscopy (EIS) for the OEC/Ta$_3$N$_5$ photoanodes was conducted at 1.23 V_{RHE} under AM 1.5G illumination (Figure 4e). The Nyquist plots were characterized by two semicircles, which were fitted using an equivalent circuit consisting of a series resistance (R_s), a charge transfer resistance in the semiconductor (R_{sc}), a charge transfer resistance at the photoanode/electrolyte interface (R_{ct}), and their corresponding constant phase elements (CPE_{sc} and CPE_{ct}) (inset of Figure 4e).[54,55] The fitted R_{ct} presents that the N:CoFeO$_x$/Ta$_3$N$_5$ (68.20 Ω cm^2) shows a smaller R_{ct} than CoFeO$_x$/Ta$_3$N$_5$ (116.1 Ω cm^2) and CoO$_x$/Ta$_3$N$_5$ (167.2 Ω cm^2), implying a more efficient interfacial charge transfer (Table S1, Supporting Information). Furthermore, to assess the electrocatalytic activity that led to a decrease in R_{ct}, their electrochemical properties under dark conditions were examined using OEC/FTO. In Figure 4f, the N:CoFeO$_x$/FTO exhibited a relatively steep slope and a noticeable low overpotential. Therefore, these results obviously show that the N:CoFeO$_x$ modification can facilitate the transport of holes generated from Ta$_3$N$_5$ and enhance injection kinetics for water oxidation.

2.5. Charge Carrier Dynamics

For a deeper understanding of charge carrier recombination and transfer kinetics, V_{oc} measurements were conducted by generating enough photogenerated charge carriers under illumination for 10 min and then turning off the light. As evident from **Figure 5a**, the OEC/Ta$_3$N$_5$ junction significantly reduces the difference between $V_{oc,\,dark}$, and 1.23 V_{RHE} in comparison to pristine Ta$_3$N$_5$. This implies the deactivation of surface states on Ta$_3$N$_5$ and the alleviation of Fermi-level pinning.[56] The surface modification with the OEC layer could effectively prevent potential drops across the Helmholtz layer and activated band bending. When examining the differences in V_{ph} among the co-catalysts, they clearly demonstrate higher V_{ph} values than pristine Ta$_3$N$_5$. Upon closer inspection, the similar V_{ph} values of the CoFeO$_x$/Ta$_3$N$_5$ and CoO$_x$/Ta$_3$N$_5$ photocathodes suggest that the difference in onset potential between the two co-catalysts is not attributed to energetic factors.[57] In essence, the difference might be traced to changes in the kinetic factor of the OER process. Of particular note is the observation that the integration of N-species into the CoFeO$_x$ matrix results in a significant increase in photovoltage, with N:CoFeO$_x$/Ta$_3$N$_5$ achieving the highest photovoltage of 0.534 V. This higher hole flux into N:CoFeO$_x$ could be explained by its capacity to suppress recombination losses and promote charge separation through the long-lived photogenerated holes.[58] To explicate the charge recombination rate, we extracted the lifetime of charge carriers as a function of V_{oc} (Figure 5b), according to following the equation:[59]

$$\tau_n = -\frac{\kappa_B T}{e}\left(\frac{dV_{oc}}{dt}\right)^{-1} \quad (1)$$

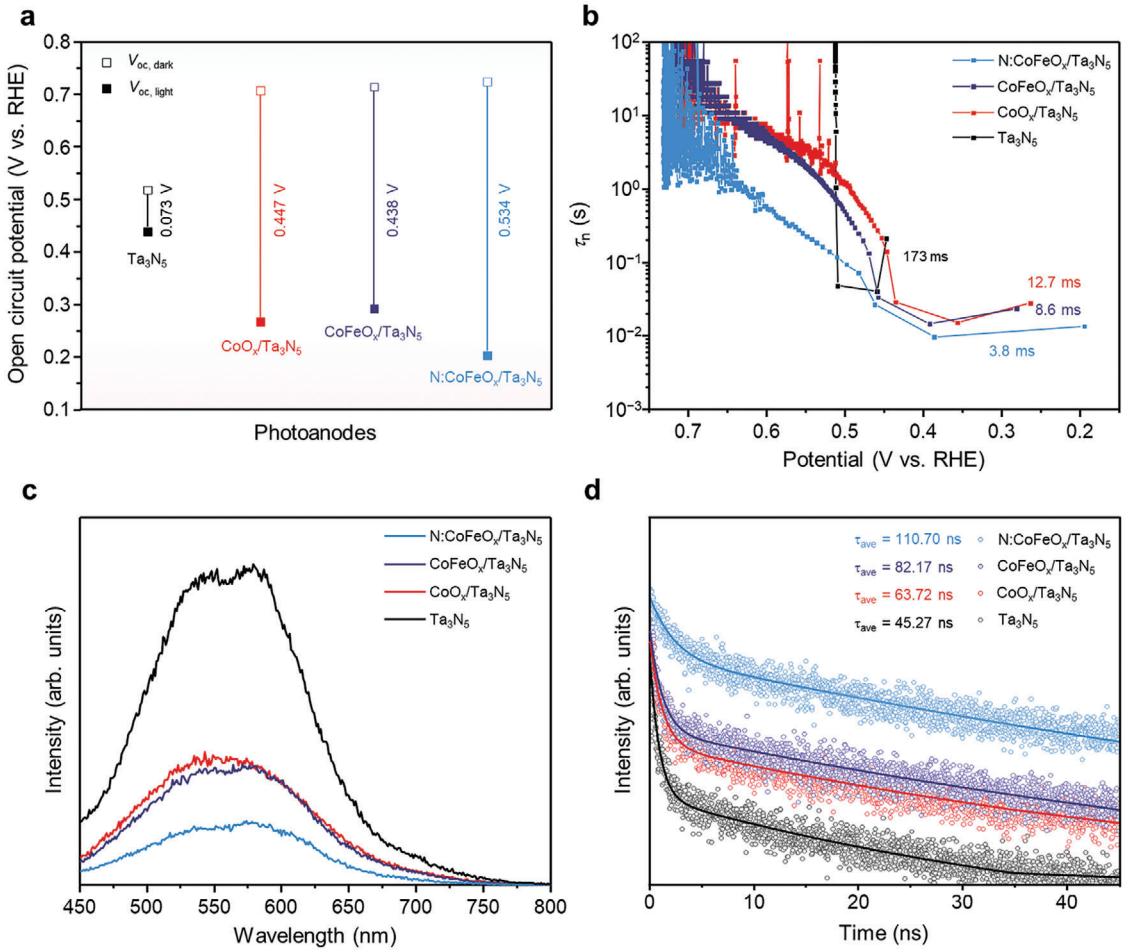

Figure 5. a) Open circuit potential (V_{oc}) in the dark and illumination and b) Carrier lifetimes derived from V_{oc} -decay curves at the light on-off transient for $N:CoFeO_x/Ta_3N_5/NbN_x$/n-Si, $CoFeO_x/Ta_3N_5/NbN_x$/n-Si, $CoO_x/Ta_3N_5/NbN_x$/n-Si, and pristine Ta_3N_5/NbN_x/n-Si. c) steady-state PL spectra, and d) TRPL spectra at 590 nm for $N:CoFeO_x/Ta_3N_5/NbN_x$/n-Si, $CoFeO_x/Ta_3N_5/NbN_x$/n-Si, $CoO_x/Ta_3N_5/NbN_x$/n-Si, and pristine Ta_3N_5/NbN_x/n-Si.

where τ_n, κ_B, T, e, and dV_{oc}/dt are the carrier lifetime, Boltzmann's constant, temperature (K), charge of a single electron, and derivative of the V_{oc} transient decay, respectively. As shown in Figure 5b, $N:CoFeO_x/Ta_3N_5$ has a fast carrier lifetime of 3.8 ms, which is lower than those of $CoFeO_x/Ta_3N_5$ (8.6 ms), CoO_x/Ta_3N_5 (12.7 ms), and Ta_3N_5 (173 ms). A short carrier lifetime implies that carrier relaxation occurs rapidly when illumination is blocked, conversely indicating that photogenerated carriers transfer rapidly into the OEC layer under illumination. The rapid decay kinetics of $N:CoFeO_x/Ta_3N_5$ validate its capability to reduce the charge trapping and improve separation and injection.

Furthermore, the steady-state photoluminescence (PL) spectra and time-resolved PL (TRPL) decay spectra were conducted to characterize the dynamics of photogenerated charge carriers qualitatively. Figure 5c shows an emission peak derived from band-to-band transition at ca. 590 nm. This PL peak represents a broad emission peak resulting from radiative recombination due to the defect states within Ta_3N_5.[60] The addition of the OEC layer consistently resulted in successful PL emission quenching compared to the pristine Ta_3N_5, with the most dramatic effect observed in the $N:CoFeO_x/Ta_3N_5$ photoanode. The lowest intensity of PL intensity correlates to the inhibition of charge recombination and enhancement of charge separation, resulting in the same results as the V_{oc}-decay derived carrier lifetimes discussed above. The charge carrier lifetimes are further evaluated by TRPL spectra measured at 590 nm (Figure 5d). The TRPL decay spectra were fitted by a biexponential decay function to capture the initial fast decay and the subsequent slow decay.[20,61] These fitting results are listed in Table S2 (Supporting Information). The τ_1 values, the fast decay component attributed to defect-related electron trapping, are similar for the various photoanodes. In contrast, there was a noticeable difference in the τ_2 values, corresponding to the slow decay component attributed to electron-hole recombination. Consequently, the intensity-weighted average lifetime τ_{ave} of $N:CoFeO_x/Ta_3N_5$ photoanode (110.70 ns) is longer than that of $CoFeO_x/Ta_3N_5$ (82.17 ns), CoO_x/Ta_3N_5 (63.72 ns), and Ta_3N_5 (45.27 ns), indicating a connection with the charge storage ability of low-valence transition metals as confirmed by XPS analysis. We can therefore conclude that $N:CoFeO_x$ serves as a shelter for long-lived holes before being employed for water oxidation, retarding the recombination of photogenerated holes in Ta_3N_5.[62,63] This

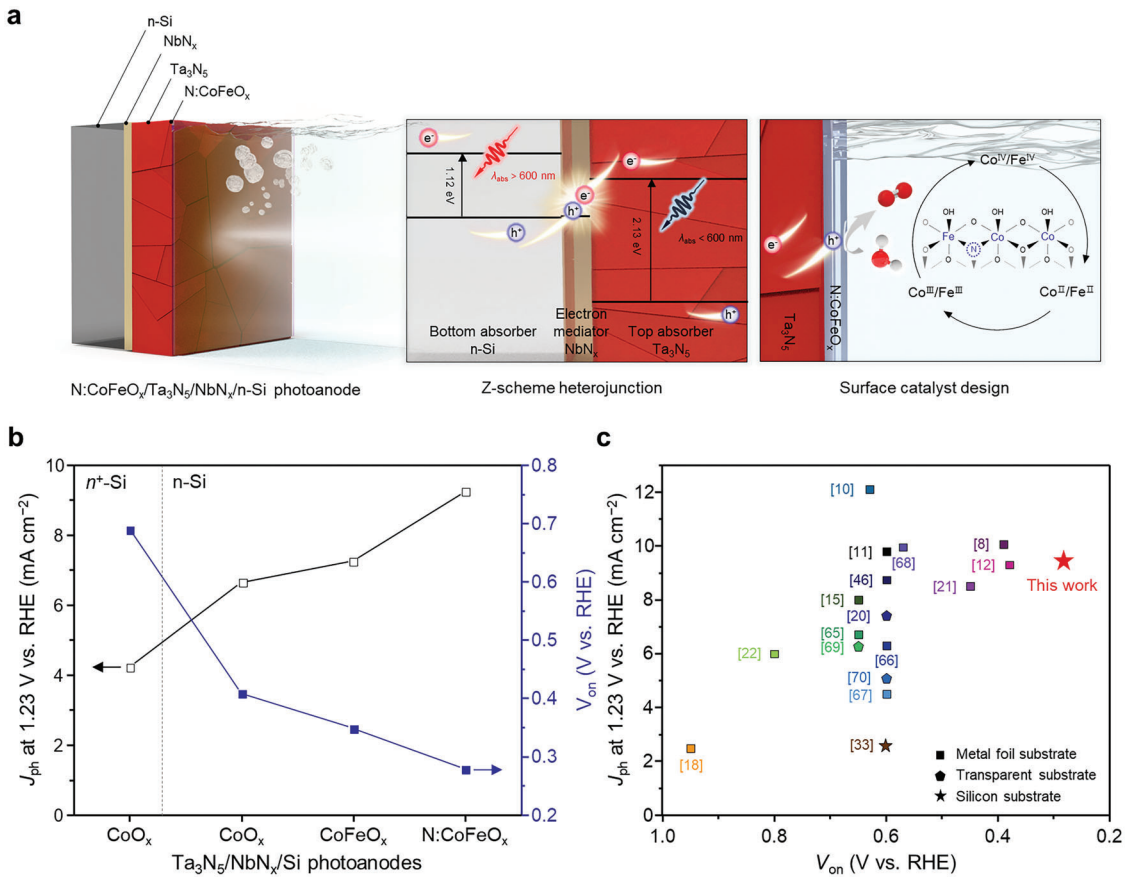

Figure 6. a) Schematic illustration of the N:$CoFeO_x$/Ta_3N_5/NbN_x/n-Si photoanode during PEC water oxidation. b) J_{ph} at 1.23 V versus RHE and V_{on} of the CoO_x/Ta_3N_5/NbN_x/n^+-Si, CoO_x/Ta_3N_5/NbN_x/n-Si, $CoFeO_x$/Ta_3N_5/NbN_x/n-Si, and N:$CoFeO_x$/Ta_3N_5/NbN_x/n-Si photoanode. c) Summary of J_{ph} at 1.23 V versus RHE and V_{on} with recently reported Ta_3N_5 photoanodes.

TRPL analysis suggests that the reduced recombination losses in N:$CoFeO_x$/Ta_3N_5 are responsible for the lower onset potential and higher photocurrent densities, facilitating the participation of more holes in the water oxidation reaction.

3. Conclusion

In summary, the N:$CoFeO_x$/Ta_3N_5/NbN_x/n-Si photoanode has provided an archetype to integrate two strategies of the Z-schematic heterojunction and the N:$CoFeO_x$ OEC design, effectively enhancing PEC activity in water oxidation. To elucidate the optical factors and charge transport pathways associated with PEC performance, we conscientiously examined the roles of each light absorber, Ta_3N_5 and n-Si, and their synergy. By constructing and optimizing of the NbN_x electron mediator and n-Si with enlarged band bending, this concerted photoelectrode exhibited outstanding light utilization capabilities, achieving photovoltage augmentation. Further on, the N:$CoFeO_x$ OEC provided the prolonged carrier lifetime and improved reaction kinetics originating from divalent transition metals, successfully transporting photogenerated holes from Ta_3N_5 to electrocatalysis and accelerating the onset of the photocurrent (**Figure 6a**). As summarized in Figure 6b, this integration of Ta_3N_5 and n-Si resulted in a cumulative increase in photovoltage, which led to a 40% reduction in V_{on} and an increase in J_{ph} by 57% compared to n^+-Si. In addition, with the consecutive introduction of dual metal oxides and N-substitutional defects, the N:$CoFeO_x$ OEC further reduced V_{on} by 34% (0.27 V_{RHE}) and increased J_{ph} by 39% (9.28 mA cm^{-2}). This exceptionally fast V_{on} of the N:$CoFeO_x$/Ta_3N_5/NbN_x/n-Si photoanode surpassed previous works on Ta_3N_5-based photoanode for PEC water oxidation reactions (Figure 6c).[8,10–12,14,17,19–21,32,45,64–69] We demonstrated for the first time a Ta_3N_5-Si heterojunction with a metallic charge mediator, broadening the substrate exploitation in Ta_3N_5 photoanode development. Furthermore, we have proposed a new strategy for OEC modification to drive charge carriers in Ta_3N_5 toward water oxidation competently. We believe that our approach provides a novel structural perspective in the design of high-efficiency PEC configurations in solar water-splitting systems.

4. Experimental Section

Fabrication of Ta_3N_5/Si and Ta_3N_5/NbN_x/Si: The moderately phosphorous doped crystalline n-Si wafer (<100> orientation, resistivity 1–10 Ω cm, 525 ± 15 µm thick, single side polished), and highly doped n^+-Si wafer (<100> orientation, resistivity 0.001–0.005 Ω cm, 525 ± 15 µm thick, single side polished) were cut into pieces with a size of 1 × 1 cm.

The Si wafers were cleaned sequentially in an ultrasonic bath of acetone, isopropanol, and deionized water for 20 min. Next, the Si wafers were immersed in a diluted HF solution for 1 min to remove the native oxide layer, followed by rinsing with deionized water and drying with flowing N_2. The Nb_2O_5 layer with 10–30 nm thickness was deposited immediately by electron-beam evaporation with a deposition rate of 0.2 Å s^{-1} at a 5.0×10^{-6} Torr pressure. In the structure without NbN_x interlayer, Ta_2O_5 film was directly deposited. The Ta_2O_5 layer with 600 nm thickness was deposited by electron-beam evaporation with a deposition rate of 1.0 Å s^{-1} at a pressure of 2.0×10^{-5} Torr. After the deposition, Ta_3N_5/Si and Ta_3N_5/NbN_x/Si were obtained by one-step thermal nitridation. The as-deposited oxide films were transferred into the quartz tube furnace and purged by N_2 for 30 min. Subsequently, the quartz tube was purged by NH_3 (99.999%) with a flow rate of 250 sccm. Under the same flow rate, the samples were nitridated at a temperature of 950 °C for 150 min with a ramping rate of 5 °C min^{-1} and cooled down naturally to room temperature.

Synthesis of N:CoFeO$_x$, CoFeO$_x$, and CoO$_x$ Co-Catalysts: The $CoFeO_x$ and CoO_x OER co-catalysts were deposited on the surface of Ta_3N_5/NbN_x/Si photoanode using the drop-casting method. The precursor solution was prepared by dissolving cobalt(II) 2-ethylhexanoate (Sigma-Aldrich, 65%w/w in mineral spirits) and iron(III) 2-ethylhexanoate (Alfa Aesar, 50%w/w in mineral spirits) in *n*-hexane (Acros, 99%) to have a total metal complex concentration of 15% w/w. The composition of $CoFeO_x$ was controlled by adjusting the Co and Fe precursor ratio. A 30 µl cm^{-2} precursor solution was directly dropped on the surface of the photoanode. After drying in the air for 5 min, the samples were then annealed at 140 °C on a heating plate in the air for 45 min. The N:$CoFeO_x$/Ta_3N_5 and N:CoO_x/Ta_3N_5 photoanodes were prepared using N_2 plasma treatment for 5 min with customized plasma equipment (Femto-Science, CUTE) under the following conditions: power (10 W), frequency (50 kHz), and pressure (10^{-1} Torr). The samples used to evaluate electrocatalytic properties were also synthesized in the same way using the FTO glass substrates.

Characterizations: The crystal structures of the Ta_3N_5/NbN_x/Si and Ta_3N_5/Si photoanodes were determined by X-ray diffractometer (XRD) (D8 Advance, Bruker) with Cu Kα radiation. The samples were characterized by a field-emission scanning electron microscope (SEM) (MERLIN Compact, ZEISS). The transmission electron microscope (TEM) (JEM-2100F, JEOL) analysis was conducted at an acceleration voltage of 200 kV. The TEM specimen was prepared by focused ion beam (FIB) (SMI3050SE, SII Nanotechnology) to investigate the cross-sectional structure of the photoanodes. The band structure was analyzed by ultraviolet photoelectron spectroscope (UPS) (AXIS-SUPRA, Kratos) under He I radiation (21.2 eV). The secondary electron cut-off ($E_{cut\text{-}off}$) was determined by extrapolation to the linear part of the high binding energy region. The Fermi level (E_f) was calculated by the difference between the E_{cutoff} and He I photon source energy of 21.2 eV. The valence band edge (E_{edge}) is the difference between E_f and valence band maximum (E_{VBM}), determined by extrapolation to the linear part of the low binding energy region. The absorption and transmittance spectra of Ta_3N_5 and Ta_3N_5/NbN_x films were obtained by a UV–vis spectrometer (V-770, JASCO). The surface chemical states of the N:$CoFeO_x$/Ta_3N_5 and $CoFeO_x$/Ta_3N_5 were analyzed using an X-ray photoelectron spectroscope (XPS) (AXIS-His, Kratos) with a monochromatic Mg Kα X-ray source. The binding energy was calibrated by setting the binding energy of hydrocarbon C 1 s peak at 284.8 eV. The narrow spectrums were analyzed using CASA XPS software. The PL and TRPL analyses were conducted at a laser excitation wavelength of 405 nm using a fluorescence spectrophotometer (FlouTime 300, PicoQuant).

Photoelectrochemical Measurements: All PEC measurements were conducted on a potentiostat (Nstat, Ivium Technologies) in 1 M KOH (pH 13.6) with a three-electrode system. A saturated Ag/AgCl reference electrode and a Pt mesh counter electrode were used. To fabricate the working electrode for PEC measurements, ohmic contact was formed on the backside of the Si substrate. In detail, the oxide on the backside was removed using an electric drill; then a Ga-In eutectic alloy (Sigma–Aldrich, 99.99%) was applied, and Ag paste was used on the scratched part to connect the sample and the Cu wire electrically. Finally, the sample was encapsulated with epoxy (Loctite EA 9492), leaving an exposed active area of ≈0.05 cm^2. A solar simulator with an Xe arc lamp (LS150, Abet Technologies) was used as a light source, and the irradiance was calibrated to AM 1.5G illumination (100 mW cm^{-2}, 1 sun) using a standard silicon photodiode. The measured potentials were converted to the reversible hydrogen electrode (RHE) using the following equation:

$$E_{RHE} = E_{Ag/AgCl} + 0.059 \times pH + E^{\circ}_{Ag/AgCl} \quad (2)$$

where $E_{Ag/AgCl}$ is the measured potential versus the Ag/AgCl reference electrode, and $E^{\circ}_{Ag/AgCl}$ is 0.198 V at 25 °C. All *J*–*V* measurements were performed between 0.2 and 1.5 V_{RHE} at a scan rate of 20 mV s^{-1}. Filtered light illumination was achieved using a 600 nm long wavelength pass filter and a 600 nm short wavelength pass filter (Edmund Optics), allowing selective irradiation of the desired wavelength range while maintaining the intensity under AM 1.5G illumination. The open circuit potential (V_{oc}) versus elapsed time under chopped illumination was performed in a continuous on-off state for 20 s each, sequentially under the following conditions: AM 1.5G simulated full spectrum illumination, 600 nm short wavelength pass filter condition, and 600 nm long wavelength pass filter condition. The PEC stability was investigated by *J*–*t* curves at a constant applied voltage of 1.23 V_{RHE}. The Faradaic efficiency of oxygen production was calculated by gas chromatography (7890B, Agilent) under 1 sun illumination in a gas-tight H-cell at 1.23 V_{RHE}. The half-cell solar-to-hydrogen conversion efficiency (HC-STH) was calculated based on the *J*–*V* curves under AM 1.5G illumination using the following equation:

$$HC-STH\ (\%) = \left[J \times \frac{1.23 - V_{app}}{P_{light}} \right] \times 100\% \quad (3)$$

where V_{app} is the applied potential versus RHE, *J* is the photocurrent density, and P_{light} is the irradiance of the simulated sunlight (100 mW cm^{-2}). To evaluate the charge injection and separation, the hole scavenger method was used. The injection efficiency (η_{inj}) and separation efficiency (η_{sep}) were calculated using the following equations:

$$\eta_{inj} = \frac{J_{H_2O}}{J_{Na_2SO_3}} \times 100\% \quad (4)$$

$$\eta_{sep} = \frac{J_{Na_2SO_3}}{J_{abs}} \times 100\% \quad (5)$$

where J_{H_2O} and $J_{Na_2SO_3}$ are the photocurrent densities obtained in 1 M KOH electrolytes without and with 0.5 M Na_2SO_3, respectively. Absorption photocurrent density (J_{abs}) was the expected photocurrent density when absorbed photons are completely converted into current:

$$J_{abs} = \int \frac{\lambda}{1240} \Phi_{\lambda} \left[1 - 10^{-A} \right] d\lambda \quad (6)$$

where λ, Φ_{λ}, and *A* stand for the photon wavelength, photon flux of solar spectrum (AM 1.5G), and absorbance of photoanode, respectively.

Electrochemical impedance spectroscopy (EIS) was conducted with a frequency range from 100 kHz to 0.1 Hz frequency under AM 1.5G illumination at 1.23 V_{RHE} with an AC amplitude of 10 mV. The measured EIS data were fitted to equivalent circuits using Z view software. Cyclic voltametry (CV) measurements for evaluating electrocatalytic properties were conducted between 1.3 and 1.7 V_{RHE} at a scan rate of 5 mV s^{-1} with *iR*-correction.

Supporting Information

Supporting Information is available from the Wiley Online Library or from the author.

Acknowledgements

This work was supported by the National Research Foundation of Korea (NRF) funded by the Korea government Ministry of Science and ICT (MSIT) (2021M3H4A1A03057403, 2022M3H4A1A01011993). This work was also supported by the Korea Research Institute of Standards and Science (KRISS) MPI Lab. Program. The Inter-University Semiconductor Research Center and Institute of Engineering Research at Seoul National University provided research facilities for this work.

Conflict of Interest

The authors declare no conflict of interest.

Data Availability Statement

The data that support the findings of this study are available from the corresponding author upon reasonable request.

Keywords

photoelectrochemical water oxidation, photovoltages, tantalum nitride photoanodes, Z-scheme

Received: October 4, 2023
Revised: November 19, 2023
Published online:

[1] M. Grätzel, *Nature* **2001**, *414*, 338.
[2] N S. Lewis, *Science* **2016**, *351*, aad1920.
[3] Q. Wang, C. Pornrungroj, S. Linley, E. Reisner, *Nat. Energy* **2022**, *7*, 13.
[4] P. Zhang, T. Wang, J. Gong, *Chem* **2018**, *4*, 223.
[5] J. H. Kim, D. Hansora, P. Sharma, Ji-W Jang, J. S. Lee, *Chem. Soc. Rev.* **2019**, *48*, 1908.
[6] S. Corby, R R. Rao, L. Steier, J R. Durrant, *Nat. Rev. Mater.* **2021**, *6*, 1136.
[7] J. Seo, H. Nishiyama, T. Yamada, K. Domen, *Angew. Chem.* **2018**, *130*, 8530.
[8] Y. Xiao, Z. Fan, M. Nakabayashi, Q. Li, L. Zhou, Q. Wang, C. Li, N. Shibata, K. Domen, Y. Li, *Nat. Commun.* **2022**, *13*, 7769.
[9] Y. Pihosh, V. Nandal, R. Shoji, R. Bekarevich, T. Higashi, V. Nicolosi, H. Matsuzaki, K. Seki, K. Domen, *ACS Energy Lett.* **2023**, *8*, 2106.
[10] G. Liu, S. Ye, P. Yan, F. Xiong, P. Fu, Z. Wang, Z. Chen, J. Shi, C. Li, *Energy Environ. Sci.* **2016**, *9*, 1327.
[11] P. Wang, C. Ding, Y. Deng, H. Chi, H. Zheng, L. Liu, H. Li, Y. Wu, X. Liu, J. Shi, C. Li, *ACS Catal.* **2023**, *13*, 2647.
[12] J. Fu, Z. Fan, M. Nakabayashi, H. Ju, N. Pastukhova, Y. Xiao, C. Feng, N. Shibata, K. Domen, Y. Li, *Nat. Commun.* **2022**, *13*, 729.
[13] X. Yang, C. Du, R. Liu, J. Xie, D. Wang, *J. Catal.* **2013**, *304*, 86.
[14] M. Zhong, T. Hisatomi, Y. Sasaki, S. Suzuki, K. Teshima, M. Nakabayashi, N. Shibata, H. Nishiyama, M. Katayama, T. Yamada, K. Domen, *Angew. Chem.* **2017**, *129*, 4817.
[15] B. Zhang, Z. Fan, Y. Chen, C. Feng, S. Li, Y. Li, *Angew. Chem., Int. Ed.* **2023**, *62*, e202305123.
[16] Y. Zhao, G. Liu, H. Wang, Y. Gao, T. Yao, W. Shi, C. Li, *J. Mater. Chem. A* **2021**, *9*, 11285.
[17] P. Zhang, T. Wang, J. Gong, *Chem. Commun.* **2016**, *52*, 8806.
[18] G. Liu, J. Shi, F. Zhang, Z. Chen, J. Han, C. Ding, S. Chen, Z. Wang, H. Han, C. Li, *Angew. Chem., Int. Ed.* **2014**, *53*, 7295.
[19] T. Higashi, H. Nishiyama, V. Nandal, Y. Pihosh, Y. Kawase, R. Shoji, M. Nakabayashi, Y. Sasaki, N. Shibata, H. Matsuzaki, K. Seki, K. Takanabe, K. Domen, *Energy Environ. Sci.* **2022**, *15*, 4761.
[20] Y. Xiao, C. Feng, J. Fu, F. Wang, C. Li, V F. Kunzelmann, C.-M. Jiang, M. Nakabayashi, N. Shibata, I D. Sharp, K. Domen, Y. Li, *Nat. Catal.* **2020**, *3*, 932.
[21] Y. He, P. Ma, S. Zhu, M. Liu, Qi Dong, J. Espano, X. Yao, D. Wang, *Joule* **2017**, *1*, 831.
[22] P. Chakthranont, T R. Hellstern, J M. Mcenaney, T F. Jaramillo, *Adv. Energy Mater.* **2017**, *7*, 1701515.
[23] S. Hu, C. Xiang, S. Haussener, A D. Berger, N S. Lewis, *Energy Environ. Sci.* **2013**, *6*, 2984.
[24] M S. Prévot, K. Sivula, *J. Phys. Chem. C* **2013**, *117*, 17879.
[25] Y. J. Hwang, A. Boukai, P. Yang, *Nano Lett.* **2009**, *9*, 410.
[26] S. Y. Noh, Ke Sun, C. Choi, M. Niu, M. Yang, Ke Xu, S. Jin, D. Wang, *Nano Energy* **2013**, *2*, 351.
[27] Z. Zhou, S. Wu, L. Qin, L. Li, L. Li, X. Li, *J. Mater. Chem. A* **2018**, *6*, 15593.
[28] Li Chen, S. Wu, D. Ma, A. Shang, X. Li, *Nano Energy* **2018**, *43*, 177.
[29] M T. Mayer, C. Du, D. Wang, *J. Am. Chem. Soc.* **2012**, *134*, 12406.
[30] Y. Zhao, G. Brocks, H. Genuit, R. Lavrijsen, M A. Verheijen, A. Bieberle-Hütter, *Adv. Energy Mater.* **2019**, *9*, 1900940.
[31] Y. Zhao, P. Westerik, R. Santbergen, E. Zoethout, H. Gardeniers, A. Bieberle-Hütter, *Adv. Funct. Mater.* **2020**, *30*, 1909157.
[32] I. Narkeviciute, P. Chakthranont, A J. M. Mackus, C. Hahn, B A. Pinaud, S F. Bent, T F. Jaramillo, *Nano Lett.* **2016**, *16*, 7565.
[33] Y. Tachibana, L. Vayssieres, J R. Durrant, *Nat. Photonics* **2012**, *6*, 511.
[34] T. Yao, X. An, H. Han, J. Q. Chen, C. Li, *Adv. Energy Mater.* **2018**, *8*, 1800210.
[35] M. Ebihara, T. Ikeda, S. Okunaka, H. Tokudome, K. Domen, K. Katayama, *Nat. Commun.* **2021**, *12*, 3716.
[36] H. Tada, T. Mitsui, T. Kiyonaga, T. Akita, K. Tanaka, *Nat. Mater.* **2006**, *5*, 782.
[37] K. Iwashina, A. Iwase, Y. H. Ng, R. Amal, A. Kudo, *J. Am. Chem. Soc.* **2015**, *137*, 604.
[38] C. Wang, T. Hisatomi, T. Minegishi, M. Nakabayashi, N. Shibata, M. Katayama, K. Domen, *J. Mater. Chem. A* **2016**, *4*, 13837.
[39] A. Dabirian, R. Van De Krol, *Chem. Mater.* **2015**, *27*, 708.
[40] T. Yao, R. Chen, J. Li, J. Han, W. Qin, H. Wang, J. Shi, F. Fan, C. Li, *J. Am. Chem. Soc.* **2016**, *138*, 13664.
[41] F. Le Formal, M. Grätzel, K. Sivula, *Adv. Funct. Mater.* **2010**, *20*, 1099.
[42] H. Zhang, D. Li, W. J. Byun, X. Wang, T. J. Shin, Hu Y Jeong, H. Han, C. Li, J. S. Lee, *Nat. Commun.* **2020**, *11*, 4622.
[43] J. Fu, F. Wang, Y. Xiao, Y. Yao, C. Feng, Le Chang, C.-M. Jiang, V F. Kunzelmann, Z M. Wang, A O. Govorov, I D. Sharp, Y. Li, *ACS Catal.* **2020**, *10*, 10316.
[44] J. Lin, X. Han, S. Liu, Y. Lv, X. Li, Y. Zhao, Y. Li, L. Wang, S. Zhu, *Appl. Catal. B* **2023**, *320*, 121947.
[45] X. Zhang, H. Guo, G. Dong, Y. Zhang, G. Lu, Y. Bi, *Appl. Catal. B* **2020**, *277*, 119217.
[46] S. Guo, Y. Wu, C. Wang, Y. Gao, M. Li, B. Zhang, C. Liu, *Nat. Commun.* **2022**, *13*, 5297.
[47] S. Zhang, M. Li, J. Li, Q. Song, X. Liu, *Proc. Natl. Acad. Sci.* **2022**, *119*, e2115504119.
[48] L. Wang, B. Zhang, Q. Rui, *ACS Catal.* **2018**, *8*, 10564.
[49] L. Zheng, W. Ye, Y. Zhao, Z. Lv, X. Shi, Qi Wu, X. Fang, H. Zheng, *Small* **2023**, *19*, 2205092.
[50] B. Zhang, S. Yu, Y. Dai, X. Huang, L. Chou, G. Lu, G. Dong, Y. Bi, *Nat. Commun.* **2021**, *12*, 6969.
[51] Y. Dai, P. Cheng, G. Xie, C. Li, M. Z. Akram, B. Guo, R. Boddula, X. Shi, J. Gong, J Ru Gong, *J. Phys. Chem. C* **2019**, *123*, 28753.
[52] B. Klahr, S. Gimenez, F. Fabregat-Santiago, J. Bisquert, T W. Hamann, *J. Am. Chem. Soc.* **2012**, *134*, 16693.
[53] Y. He, J. E. Thorne, C. H. Wu, P. Ma, C. Du, Qi Dong, J. Guo, D. Wang, *Chem* **2016**, *1*, 640.

[54] G. Xie, X. Liu, B. Guo, T. Tan, J Ru Gong, *Adv. Mater.* **2023**, 2211008.
[55] J. Deng, Y. Li, Y. Xiao, K. Feng, C. Lu, K. Nie, X. Lv, H. Xu, J. Zhong, *ACS Catal.* **2022**, *12*, 7833.
[56] J. Wang, G. Ni, W. Liao, K. Liu, J. Chen, F. Liu, Z. Zhang, M. Jia, J. Li, J. Fu, E. Pensa, L. Jiang, Z. Bian, E. Cortés, M. Liu, *Angew. Chem., Int. Ed.* **2023**, *62*, e202217026.
[57] Z. Jiang, X. Zhu, Z. Wang, W. Liu, W. Yan, K. Sivula, J. Bao, *Adv. Sci.* **2023**, *10*, 230869.
[58] B. Moss, F. S. Hegner, S. Corby, S. Selim, L. Francàs, N. López, S. Giménez, J.-R. Galán-Mascarós, J. R. Durrant, *ACS Energy Lett.* **2019**, *4*, 337.
[59] M. Zhong, T. Hisatomi, Y. Kuang, J. Zhao, M. Liu, A. Iwase, Q. Jia, H. Nishiyama, T. Minegishi, M. Nakabayashi, N. Shibata, R. Niishiro, C. Katayama, H. Shibano, M. Katayama, A. Kudo, T. Yamada, K. Domen, *J. Am. Chem. Soc.* **2015**, *137*, 5053.
[60] Y. Xie, Y. Wang, Z. Chen, X. Xu, *ChemSusChem* **2016**, *9*, 1403.
[61] R.-T. Gao, S. Liu, X. Guo, R. Zhang, J. He, X. Liu, T. Nakajima, X. Zhang, L. Wang, *Adv. Energy Mater.* **2021**, *11*, 2102384.
[62] M. Barroso, A J. Cowan, S R. Pendlebury, M. Grätzel, D R. Klug, J R. Durrant, *J. Am. Chem. Soc.* **2011**, *133*, 14868.
[63] M. Barroso, C A. Mesa, S R. Pendlebury, A J. Cowan, T. Hisatomi, K. Sivula, M. Grätzel, D R. Klug, J R. Durrant, *Proc. Natl. Acad. Sci. U. S. A.* **2012**, *109*, 15640.
[64] Y. Li, Li Zhang, A. Torres-Pardo, J M. González-Calbet, Y. Ma, P. Oleynikov, O. Terasaki, S. Asahina, M. Shima, D. Cha, L. Zhao, K. Takanabe, J. Kubota, K. Domen, *Nat. Commun.* **2013**, *4*, 2566.
[65] Z. Shi, J. Feng, H. Shan, X. Wang, Z. Xu, H. Huang, Q. Qian, S. Yan, Z. Zou, *Appl. Catal. B* **2018**, *237*, 665.
[66] Y. Pihosh?, V. Nandal, T. Minegishi, M. Katayama, T. Yamada, K. Seki, M. Sugiyama, K. Domen, *ACS Energy Lett.* **2020**, *5*, 2492.
[67] Y. Pihosh, T. Minegishi, V. Nandal, T. Higashi, M. Katayama, T. Yamada, Y. Sasaki, K. Seki, Y. Suzuki, M. Nakabayashi, M. Sugiyama, K. Domen, *Energy Environ. Sci.* **2020**, *13*, 1519.
[68] T. Higashi, H. Nishiyama, Y. Suzuki, Y. Sasaki, T. Hisatomi, M. Katayama, T. Minegishi, K. Seki, T. Yamada, K. Domen, *Angew. Chem., Int. Ed.* **2019**, *58*, 2300.
[69] Y. Kawase, T. Higashi, M. Katayama, K. Domen, K. Takanabe, *ACS Appl. Mater. Interfaces* **2021**, *13*, 16317.

